Chapter 2
Three-Dimensional Optical-Resolution Photoacoustic Microscopy

Song Hu, Konstantin Maslov, and Lihong V. Wang

Three-dimensional optical-resolution photoacoustic microscopy (OR-PAM), an emerging optical-acoustic hybrid technology capable of imaging optical absorption contrasts with subcellular resolution and sensitivity, has been recognized as a valuable complement to existing optical microscopy technologies. In this chapter, we provide detailed discussion on the design and operation of OR-PAM, including the principle, system design, system configuration, system alignment, experimental procedures, laser safety, functional imaging scheme, recent technical advances, and sample biomedical applications. Future directions of OR-PAM development are also discussed at the end of this chapter.

2.1 Introduction

The past two decades have witnessed a dramatic growth in biomedical applications of optical microscopy. Mainstream microscopy technologies—including, but not limited to, confocal microscopy, multiphoton microscopy, and optical coherence tomography (OCT)—have greatly benefited from advances in laser technology, fluorescent labeling, scanning mechanisms, and image acquisition; however, all these technologies rely on either optical scattering or fluorescent contrast and have difficulty in sensing optical absorption properties of biological tissues [1].

Recently, the photoacoustic effect has been utilized for biomedical imaging of tissue optical absorption, leading to a blooming technology—photoacoustic tomography (PAT). In PAT, the object absorbs short-pulsed or intensity-modulated optical irradiation, resulting in heating and further inducing high-frequency ultrasonic

S. Hu · K. Maslov · Lihong V. Wang (✉)
Optical Imaging Laboratory, Department of Biomedical Engineering, Washington University in St. Louis, St. Louis, MO 63130-4899, USA
e-mail: lhwang@wustl.edu

R. Liang (ed.), *Biomedical Optical Imaging Technologies*, Biological and Medical Physics, Biomedical Engineering, DOI 10.1007/978-3-642-28391-8_2,

waves, which can be detected to map optical absorption [2]. Thus, the photoacoustic effect provides an exquisite way to resolve the optical absorption distribution in biological tissue ultrasonically. Taking advantage of the much weaker ultrasonic scattering in tissues (1,000 times weaker than optical scattering), researchers have developed reconstruction-based photoacoustic computed tomography (PACT) [3] and focused-scanning-based photoacoustic microscopy (PAM) [4,5] for deep tissue imaging in the optical quasidiffusive or diffusive regime. When the spatial resolution in all directions is entirely determined by the photoacoustic wave, the technology is called acoustic-resolution PAT. Although having achieved great success, the acoustic-resolution PAT is inadequate for examining the anatomy and function of biological tissues at the cellular or subcellular level. To fill this gap, we have developed optical-resolution photoacoustic microscopy (OR-PAM), improving the lateral resolution of PAT to the cellular [6] or even subcellular scale [7]. As a unique optical absorption microscopy technology and a valuable complement to the existing technologies, OR-PAM has demonstrated broad biomedical applications since its invention [8–14]. Taking advantage of the strong optical absorption of endogenous hemoglobin, OR-PAM enables label-free, noninvasive, and volumetric microvascular imaging down to single capillaries, providing both anatomical (such as vessel diameter, connectivity, and tortuosity) and functional (such as hemoglobin oxygen saturation (sO_2) and blood flow velocity) information [8–11, 15]. With the aid of exogenous molecular contrast agents, OR-PAM is also capable of molecular imaging [13].

This chapter provides a detailed description of the design, operation, and application of OR-PAM, including the principle, system design, system configuration, system alignment, experimental procedures, laser safety, functional imaging scheme, recent technical advances, and sample biomedical applications. Future directions of OR-PAM development are also predicted at the conclusion of this chapter.

2.2 Principle and System Design

In PAM, volumetric imaging is realized by two-dimensional (2-D) raster scanning of the dual foci of optical excitation and ultrasonic detection, in combination with depth-resolved ultrasonic detection. The two foci are configured coaxially and confocally to maximize the imaging sensitivity. Thus, the lateral resolution of PAM is determined by the product of the two point spread functions.

In dark-field acoustic-resolution PAM (AR-PAM) [5], the maturest version of AR-PAM, a pulsed laser beam passes through a conical lens to form a ring-shaped illumination and then is weakly focused into biological tissues to overlap the tight ultrasonic focus [Fig. 2.1a]. Since the ultrasonic focus is smaller than the optical focus, the lateral resolution of AR-PAM is determined acoustically as [16]

$$\Delta r_{\mathrm{R}} = \frac{0.71\lambda_0}{\mathrm{NA}}, \tag{2.1}$$

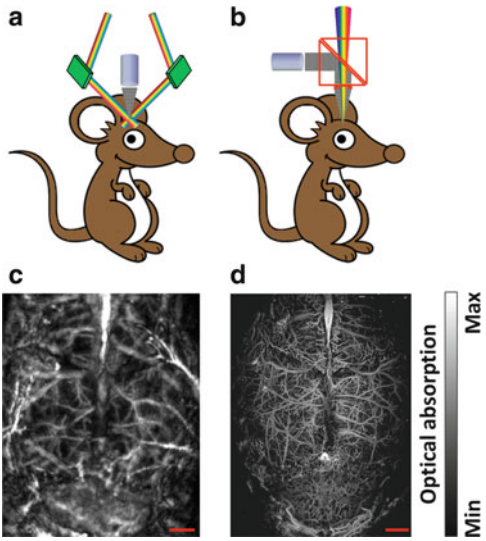

Fig. 2.1 Comparison of acoustic-resolution photoacoustic microscopy (AR-PAM) and optical-resolution photoacoustic microscopy (OR-PAM). (**a**) Schematic of AR-PAM. (**b**) Schematic of OR-PAM. (**c**) AR-PAM image of the cortical vasculature in a living adult mouse with both the scalp and the skull intact. (**d**) OR-PAM image of the cortical vasculature in a living adult mouse with the scalp removed and the skull intact. Scale bars: 1 mm

where λ_0 and NA denote the center wavelength of the photoacoustic wave and the numerical aperture of the ultrasonic detector, respectively. A lateral resolution of 45 μm has been achieved with a center frequency of 50 MHz and an NA of 0.44 [5]. This resolution, although adequate for many biomedical applications, cannot resolve fine structures such as capillaries (diameter: 4–9 μm).

To resolve single capillaries acoustically, an ultrasonic center frequency of greater than 400 MHz is required; however, at such a frequency, strong ultrasonic attenuation limits the penetration depth to less than 100 μm [6]. A more practical way to improve the lateral resolution is to use fine optical focusing. As shown in Fig. 2.1b, the optical excitation beam can be focused to a diffraction-limited spot inside the acoustic focus. Thus, the size of the optically excited region, rather than that of the ultrasonically detected region, determines the lateral resolution. Using this configuration (referred to as OR-PAM), the lateral resolution of PAM can be improved from 45 to 5 μm [6] or even better [7], at the expense of penetration depth. Figures 2.1c and d present a vivid comparison of the penetration and resolution of AR-PAM and OR-PAM [12, 17]. OR-PAM can clearly resolve as small as single capillaries in an adult mouse brain through the intact skull [Fig. 2.1d], while AR-PAM can only resolve cortical vessels thicker than 50 μm [Fig. 2.1c]. However, OR-PAM requires the scalp to be removed, while AR-PAM is able to penetrate both the scalp and the skull.

Based on the principle of OR-PAM, we list a couple of general guidelines that one may consider to follow when designing an OR-PAM system:

1. Higher optical resolution always accompanies with a smaller optical focus zone. Balance the trade-off by choosing a proper optical condenser lens or microscope objective according to the desired lateral resolution.

2. Higher-frequency ultrasonic transducer provides finer axial resolution at the expense of ultrasonic penetration. Choose a proper transducer according to the desired axial resolution and imaging depth. Generally speaking, the optimal transducer center frequency is between 50 and 150 MHz.
3. The optical and ultrasonic foci should be configured coaxially and confocally whenever possible to maximize the imaging sensitivity.

Here is an example of how to follow the guidelines. For in vivo single capillary imaging in the skin [6], a spatial resolution comparable with or smaller than the average capillary diameter (4–9 μm) is required. Thus, we choose an optical microscope objective with an NA of 0.1, which translates into a diffraction-limited focal diameter of ~3.7 μm in the operation wavelength range (500–650 nm). With such lateral resolution, OR-PAM is capable of resolving individual RBCs (average diameter: 6–8 μm) traveling along blood vessels [11]. A transducer with a center frequency of 75 MHz and a bandwidth of 80% is chosen to provide adequate axial resolution (15 μm) without encountering severe high-frequency acoustic loss in the skin [6]. Note that for transcranial imaging of cortical capillaries, the center frequency of the ultrasonic transducer should be reduced to 30–50 MHz because of the strong skull attenuation of high-frequency ultrasound [13].

2.3 System Configuration

The schematic of a representative OR-PAM system is shown in Fig. 2.2 [18]. The photoacoustic excitation source consists of a diode-pumped solid-state laser (INNOSLAB, Edgewave) and a dye laser (CBR-D, Sirah), which emits wavelength-tunable laser pulses (pulse width: 7 ns; repetition rate: <5 kHz and controlled by the external trigger signal). The pulsed laser beam is first attenuated by a neutral-density filter (NDC-50C-2M, Thorlabs) and then focused by a condenser lens (LA1131, Thorlabs), before passing through a 25-μm pinhole (P250S, Thorlabs) for spatial filtering. The pinhole is positioned slightly away from the focus of the condenser lens, where the beam size is larger than the pinhole diameter, to allow effective filtering. Then, the filtered beam is focused by a microscope objective (RMS4X, Thorlabs). The distance between the pinhole and the objective is ~400 mm, allowing sufficient beam expansion to fulfill the back aperture of the objective. This configuration gives a near-diffraction-limited optical focus (diameter: 3.7 μm). To align the optical irradiation and ultrasonic detection coaxially and confocally, we have designed an acoustic-optical beam splitter. In this beam splitter, two right-angle prisms (NT32-545, Edmund Optics) are aligned along their hypotenuses to form a cube with a thin layer (100 μm) of silicone oil (1000cSt, Clearco Products) in between. The prism glass and the silicone oil have similar optical refractive indices (1.1:1) but very different acoustic impedances (12.7:1). As a result, this beam splitter is optically transparent but acoustically reflective, thereby deflecting the

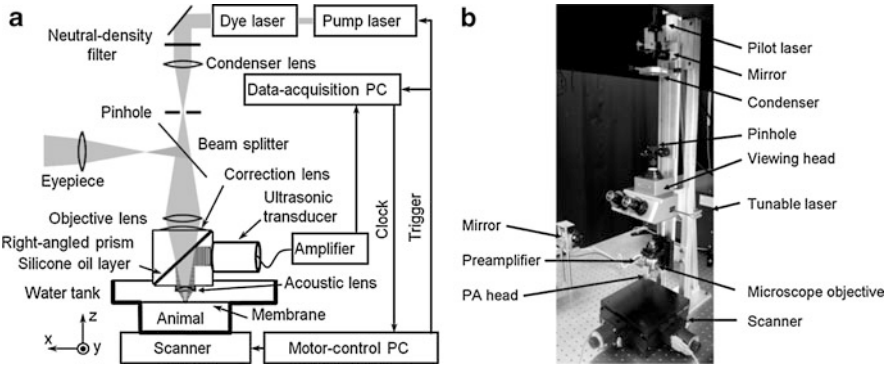

Fig. 2.2 (**a**) Schematic and (**b**) photograph of the optical-resolution photoacoustic microscopy system

acoustic axis from the optical axis by 90°. Thus, an ultrasonic transducer (V2022-BC, Olympus NDT) can be attached to the vertical side of the bottom prism for ultrasonic detection without blocking the optical irradiation, while still maintaining the coaxial alignment. An acoustic lens (geometrical radius of curvature: 5.2 mm; diameter: 6.35 mm) is attached to the bottom of the cube to be confocal with the optical irradiation. This acoustic lens has an NA of 0.46 in water and gives an acoustic focal diameter of 27 μm. To expose the imaging site, a window is opened at the bottom of the water tank and sealed with ultrasonically and optically transparent polyethylene membrane. Ultrasonic gel (Clear Image, SonoTech) is applied between the polyethylene membrane and the object for acoustic coupling. A transmission-mode optical microscope is integrated into our system by adding a white-light illumination to the object and an optical beam splitter between the pinhole and the microscope objective. Utilizing the reverse optical path of the OR-PAM, the imaging region can be viewed under the eyepiece. This addition helps quickly target the region of interest (ROI).

The photoacoustic signal detected by the ultrasonic transducer is amplified by two cascaded amplifiers (ZFL 500LN, Mini-Circuits) and then digitized by a 14-bit data acquisition (DAQ) board (CompuScope 14200, Gage Applied Sciences) at a sampling rate of 200 MS/s. Raster scanning is controlled by a separate personal computer, which triggers both the DAQ board and the pump laser. The trigger signal is synchronized with the clock-out signal from the DAQ board. The 2-D raster scanning is implemented by translating the water tank and the animal together along the horizontal (x–y) plane. The fast axis of the scanner is defined as the direction of the cross-sectional scan (B-scan). Volumetric OR-PAM image is obtained by combining a sequence of B-scan images acquired by translating the slow axis and can be viewed in direct three-dimensional (3-D) renderings or in 2-D maximum-amplitude projection (MAP) images.

2.4 System Alignment

Among the three general design guidelines, the first two are related to component selection, while the third one is about system alignment. The following acoustic-optical confocal alignment in OR-PAM is essential for high-quality imaging:

1. Use pulse-echo ultrasound and an ultrasonic reflector to determine the position of the acoustic focal plane, i.e., the time delay from the trigger signal to the maximum pulse-echo ultrasonic signal.
2. Maximize the optical power passing through the pinhole by adjusting the pinhole position within the plane perpendicular to the optical axis.
3. Check the optical diffraction pattern after the pinhole. If the beam pattern is not a clear Airy's disc surrounded by gradually fading concentric circular rings, adjust the pinhole position along the optical axis (i.e., away or towards the condenser lens) until you see the typical circular aperture diffraction pattern.
4. If the circular rings are not concentric, fine-tune the pinhole position within the plane perpendicular to the optical axis.
5. Place an optically absorbing flat target (e.g., a piece of black tape) in the acoustic focal plane.
6. Adjust the vertical position (i.e., z position) of the microscope objective to maximize the amplitude of the photoacoustic signal generated from the flat target. At the maximum, the optical focus is aligned with the acoustic focus in the vertical direction. Alternatively, users can place a 6-μm carbon fiber in the acoustic focal plane for the confocal alignment in the z direction. Repeat B-scans across the carbon fiber while adjusting the vertical position of the objective to minimize the cross-sectional diameter of the carbon fiber in the image. At the minimum, the carbon fiber is in the optical focus. Using the 6-μm carbon fiber may lead to more accurate acoustic-optical confocal alignment in the z direction.
7. With the same flat target, adjust the horizontal positions (i.e., x and y positions) of the microscope objective until the photoacoustic signal generated from the target shows a symmetric pattern as shown in Fig. 2.3. At the symmetry point, the optical focus is aligned with the acoustic focus in the horizontal direction.
8. Repeat steps 6 and 7 until the photoacoustic signal is optimized in both shape and amplitude.
9. Fix the positions of the pinhole and the microscope objective.

Note that only steps 4, 5, and 7 are required to be performed before experiments to make sure that the confocal configuration is optimized. However, if the system is found to be misaligned, users need to follow the entire procedure.

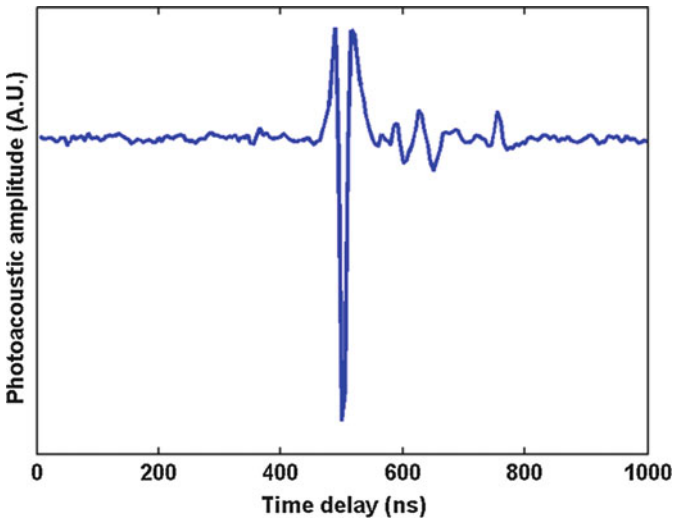

Fig. 2.3 Typical optical-resolution photoacoustic microscopy signal generated from a piece of black tape

2.5 Typical Experimental Procedures

To give readers a general idea of how to perform OR-PAM experiments, the typical procedure to image an adult mouse ear is elaborated. For other imaging applications, the procedure may be revised accordingly.

Animal depilation (if applicable):

1. Anesthetize the animal with intraperitoneal injection of a dose of 0.1 ml/10 kg cocktail (1 ml ketamine, 0.1 ml xylazine, and 8.9 ml saline).
2. Wait for 5–10 min until the animal is fully anesthetized.
3. Shave the hair in the ear.
4. Depilate the residual hair with Surgi Cream (category #: 82565, American International Industries) and clean with deionized water.

Note that the hair removal lotion may slightly irritate the animal skin, and the cocktail injection is not recommended to be used in combination with isoflurane (too much anesthesia may kill the animal). Thus, animal depilation is recommended to be performed 24 h before the planned experiment.

System preparation:

5. Turn on the photoacoustic laser system and wait for it to warm up (if applicable).
6. Seal the imaging window at the bottom of the water container with a piece of clean polyethylene membrane.
7. Fill the water container with deionized water.
8. Follow the guidelines in Sect. 2.4 to align the system.

Animal preparation:

9. Anesthetize the animal with 1% isoflurane vaporized by the inhalation gas (the typical flow rate is 1.0–1.5 l/min, depending on the animal's body weight) and maintain the anesthesia throughout the experiment. To maintain the animal under normal physiological status, the recommended inhalation gas is medical-grade air, unless other type of gas is required for specific functional studies (e.g., hypoxic challenging).
10. Fix the animal in a stereotactic stage. Set the temperature controller to the typical body temperature of mice (i.e., 37°C).
11. Flatten the mouse ear on a plastic plate and apply a layer of ultrasound gel on top of the ear. Avoid trapping air bubbles inside the gel.
12. Place the ear under the imaging window of the water tank and slowly raise the animal holder until the ultrasound gel contacts the bottom of the polyethylene membrane. Soft contact is preferred. Pressing the ear against the water tank may affect blood flow.
13. Check again to make sure no air bubble is trapped between the polyethylene membrane and the mouse ear.
14. Clamp the pulse oximeter to the animal to monitor its physiological status (recommended).
15. Apply eye ointment to the animal to prevent dryness and accidental laser damage (recommended).

Image acquisition:

16. Lower down the imaging head (i.e., the acoustic-optical beam splitter) until the acoustic lens is immersed in deionized water.
17. Remove air bubbles trapped under the acoustic lens.
18. Set the laser to the external-trigger mode and start trial scanning.
19. Adjust the z position of the imaging head until the detected photoacoustic signal is in the acoustic focal plane (judge from the acoustic delay).
20. Turn on the white-light illumination and check the imaging region under the integrated transmission-mode optical microscope. Set the scanning origin to the desired position. This is crucial for chronic monitoring, where the scanning origin should be the same position throughout the entire monitoring period.
21. Set correct scanning parameters and start image acquisition.

End experiment:

22. Turn off the laser firing once the data acquisition is completed.
23. Lift the imaging head out of water and lower down the animal holder.
24. Clean the mouse ear with deionized water, turn off the anesthesia system and the temperature controller, and unload the animal from the stereotactic stage.
25. If repetitive imaging is required, put the animal in an incubator with the temperature controlled at 37°C. Return the mouse to the animal facility after it wakes up naturally. Otherwise, follow the animal protocols to euthanatize and dispose the animal.
26. Turn off the experimental equipment and clean up the experimental area.

2.6 Functional Imaging Design

Besides the morphological information of the microvasculature that can be directly extracted from 3-D OR-PAM images, important functional and metabolic parameters, such as sO_2 and blood flow, are also measureable with specially designed imaging acquisition and data processing.

2.6.1 Spectroscopic Measurement of Oxygen Saturation of Hemoglobin

Oxyhemoglobin (HbO_2) and deoxyhemoglobin (HbR) are the two major forms of hemoglobin, the predominant endogenous photoacoustic source in the visible spectral range. HbO_2 and HbR have quite distinct optical absorption spectra and thus can be spectrally differentiated to quantify sO_2. Blood absorption imaged by label-free OR-PAM can be expressed as [19]

$$\Phi(\lambda_i) \propto \mu_a(\lambda_i) \cdot F = \ln 10 \{\varepsilon_{HbR}(\lambda_i) \cdot [HbR] + \varepsilon_{HbO_2}(\lambda_i) \cdot [HbO_2]\} \cdot F, \quad (2.2)$$

where $\mu_a(\lambda_i)$ is the blood absorption coefficient at wavelength λ_i and $\varepsilon_{HbR(HbO_2)}(\lambda_i)$ and [HbR]([HbO_2]) are the molar extinction coefficient and relative concentration of HbR (HbO_2), respectively. The detected photoacoustic signal amplitude $\Phi(\lambda_i)$ is proportional to the product of $\mu_a(\lambda_i)$ and the optical fluence F. Assuming that F is wavelength independent, we can ignore

$$\begin{bmatrix} [HbR] \\ [HbO_2] \end{bmatrix} = \begin{bmatrix} \varepsilon_{HbR}(\lambda_1) & \varepsilon_{HbO_2}(\lambda_2) \\ \varepsilon_{HbR}(\lambda_1) & \varepsilon_{HbO_2}(\lambda_2) \end{bmatrix}^{-1} \cdot \begin{bmatrix} \Phi(\lambda_1) \\ \Phi(\lambda_2) \end{bmatrix}. \quad (2.3)$$

Sequentially, sO_2 can be computed as

$$sO_2 = \frac{[HbO_2]}{[HbR] + [HbO_2]}. \quad (2.4)$$

Here are two guidelines for selecting the proper optical wavelengths to measure sO_2:

1. Wavelengths should be selected within the Q-band of hemoglobin absorption spectrum (i.e., 550–600 nm) to ensure a sufficient signal-to-noise ratio (SNR).
2. Wavelengths where ε_{HBR} and ε_{HbO_2} have a pronounced difference in their ratio (e.g., 561 nm is HbR dominant and 578 nm is HbO_2 dominant) are recommended.

Note that although a dual-wavelength measurement is adequate to calculate sO_2, using more wavelengths can potentially improve the measurement accuracy. Besides, the total hemoglobin concentration (HbT) can also be calculated in relative values, either by adding [HbR] and [HbO_2] together or by directly measuring blood

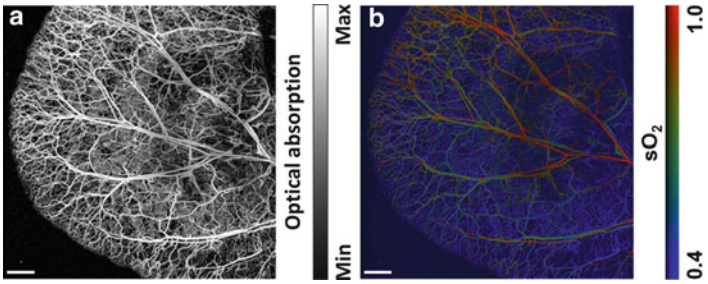

Fig. 2.4 In vivo optical-resolution photoacoustic microscopy of (**a**) vascular anatomy and (**b**) hemoglobin oxygen saturation (sO_2) in a nude mouse ear. Scale bar: 1 mm

absorption at isosbestic wavelengths (e.g., 530, 545, 570, and 584 nm) [20], where the molar extinction coefficients of HbR and HbO_2 are equal. Figure 2.4 shows the vascular anatomy and sO_2 in a nude mouse ear imaged by dual-wavelength (561 and 570 nm) OR-PAM.

2.6.2 Photoacoustic Doppler Measurement of Blood Flow Velocity

The Doppler effect, referred to the shift in wave frequency due to the relative motion between the wave source and the wave detector, has been widely used for velocity measurements. Recently, photoacoustic Doppler has been intensively studied for in vivo label-free measurement of blood flow velocity.

The prototype of photoacoustic Doppler flowmetry was invented by Fang et al. to measure the flow velocity along the acoustic axis (i.e., axial flow velocity) [21, 22]. However, within the 1 mm penetration depth of OR-PAM, biological tissues mainly form layered structures, and thus the flow component perpendicular to the acoustic axis (i.e., transverse flow) is predominant. To image transverse flow velocity, Fang et al. developed an M-mode photoacoustic particle imaging velocimetry based on OR-PAM [23]. Yao et al. further extended this technique from capillaries to all types of blood vessels with a concept called photoacoustic Doppler bandwidth broadening [15, 24].

The schematic of Doppler OR-PAM is shown in Fig. 2.5a [15]. The acoustic paths $L1$ and $L2$ subtend an obtuse angle and an acute angle with respect to the transverse flow direction, respectively. Thus, they contribute to the photoacoustic Doppler shift with opposite signs and induce bandwidth broadening. The resulting Doppler bandwidth can be computed by

$$\mathrm{PDB}_{\mathrm{OR-PAM}} = 2f_0 \cdot \frac{v_\mathrm{f}}{v_\mathrm{s}} \cdot \sin\theta \cdot \sin\varphi, \tag{2.5}$$

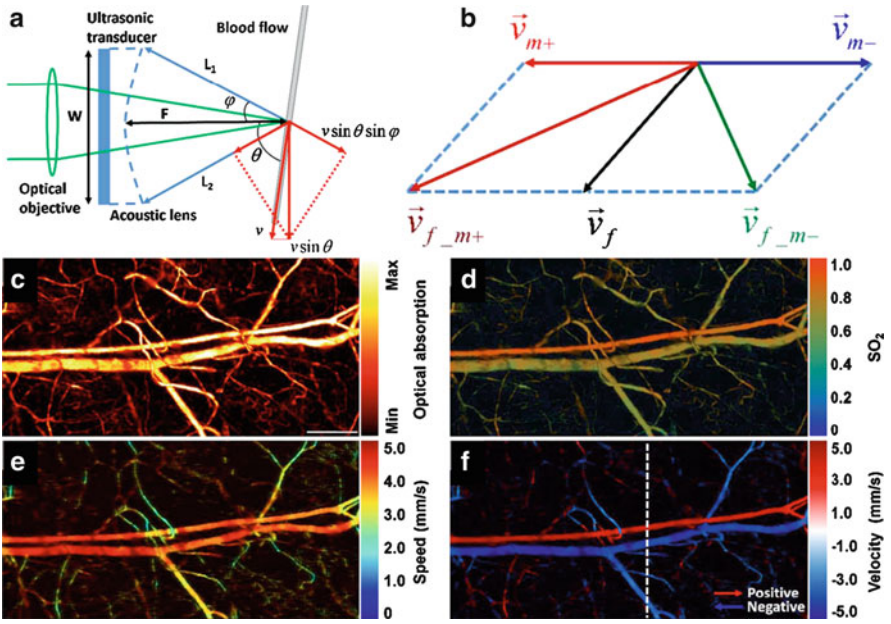

Fig. 2.5 (**a**) Schematic of the Doppler optical-resolution photoacoustic microscopy (OR-PAM). (**b**) Bidirectional scanning for flow direction sensing. OR-PAM of (**c**) vascular anatomy, (**d**) hemoglobin oxygen saturation (sO_2), (**e**) blood flow speed, and (**f**) blood flow velocity with directions in a mouse ear

where v_f is the flow speed of absorbing particles (e.g., RBCs for in vivo label-free measurement of blood flow), v_s is the speed of sound, θ is the angle subtended by the flow direction and the acoustic axis, φ is the aperture angle of the acoustic lens, and f_0 is the center frequency of the ultrasonic transducer.

Four consecutive photoacoustic A-line signals (referred to the time-resolved photoacoustic signals along the depth direction generated by individual laser pulses) are bandpass-filtered (center frequency: 75 MHz; 3-dB bandwidth: 1 MHz) and used to calculate $\mathrm{PDB}_{\mathrm{OR-PAM}}$ at each given spatial location by

$$\mathrm{PDB}_{\mathrm{OR-PAM}} = \frac{k}{T} \cdot \sqrt{1 - \frac{\left| \sum_{j=1}^{4} \tilde{p}_j \cdot \tilde{p}^*_{j+1} \right|}{\sum_{j=1}^{4} \tilde{p}_j \cdot \tilde{p}^*_j}}, \tag{2.6}$$

where T is the time interval between consecutive A-lines, k is a calibration factor, and $\tilde{p}$ is the Hilbert transform of A-line signal p. Thus, the flow speed v_f can be computed by substituting the calculated $\mathrm{PDB}_{\mathrm{OR-PAM}}$ to Eq. (2.5).

In our OR-PAM system, motor scanning also contributes to the Doppler bandwidth broadening. The measured flow speed is actually a vector combination of the flow speed and the motor-scanning speed [Fig. 2.5b]. Thus, bidirectional motor scanning can be used to determine the flow direction. The measured flow speeds under the two scanning directions are

$$v_{\mathrm{f\_m+}} = \sqrt{v_{\mathrm{f}}^2 + v_{\mathrm{m}}^2 + 2v_{\mathrm{f}} \cdot v_{\mathrm{m}} \cdot \cos\phi} \tag{2.7}$$

$$v_{\mathrm{f\_m+}} = \sqrt{v_{\mathrm{f}}^2 + v_{\mathrm{m}}^2 - 2v_{\mathrm{f}} \cdot v_{\mathrm{m}} \cdot \cos\phi}, \tag{2.8}$$

where v_{m} is the motor-scanning speed and ϕ is the angle subtended by $\vec{v}_{\mathrm{m+}}$ and $\vec{v}_{\mathrm{f}}$. Solving the simultaneous equations (2.7) and (2.8), we can get the true flow speed via

$$v_{\mathrm{f}} = \sqrt{\frac{v_{\mathrm{f\_m+}}^2 + v_{\mathrm{f\_m-}}^2 - 2v_{\mathrm{m}}^2}{2}}. \tag{2.9}$$

By comparing $v_{\mathrm{f\_m+}}$ and $v_{\mathrm{f\_m-}}$, we can further determine the flow direction.

Figure 2.5c–e shows the in vivo label-free Doppler OR-PAM imaging of a mouse ear [15]. A $1 \times 2\,\mathrm{mm}^2$ROI was bidirectionally scanned with a motor speed of 0.75 mm/s and a step size of 0.625 μm. Two optical wavelengths (560 and 570 nm) were used to image the vascular anatomy [Fig. 2.5c] and sO_2 [Fig. 2.5d]. The flow speed is pseudocolored in Fig. 2.5e, and the positive and negative flow directions are labeled red and blue in Fig. 2.5f, respectively. Determination of flow direction also helps distinguish arterioles from venules because the paired arteriole and venule are expected to have opposite flow directions [Fig. 2.5d, f].

2.7 Laser Safety

Similar to other scanning optical microscopy technologies, OR-PAM can improve SNR by increasing the pulse energy. However, for in vivo applications, laser parameters (such as optical wavelength, pulse duration, exposure duration, and exposure aperture) are regulated by laser safety standards of the American National Standards Institute (ANSI) [25].

2.7.1 Laser Safety for Ophthalmic Imaging [11, 25]

We have demonstrated OR-PAM imaging of the anterior segment of a living mouse eye [11]. The experimental parameters and ANSI-defined constants are listed as follows:

- Operation wavelengths (λ): 570 and 578 nm. Because 570 and 578 nm are close to each other and show minimal differences in terms of the safety limits, we use 570 nm throughout the calculation.
- Laser pulse repetition frequency (PRF): 600 Hz.
- Duration of a single laser pulse (t): 7 ns.
- Exposure duration of each B-scan (T_{Bscan}): 2.7 s.
- Exposure duration of a complete volumetric scan ($T_{\max}$): 7,200 s.
- Number of pulses in each B-scan (n_{Bscan}): 1,600.
- Number of pulses in the total 2-h exposure (n_{Total}): 2.56×10^6.
- Angular subtense (α): 200 mrad. The angular subtense is estimated by the NA of the microscope objective, which is 0.1 in our current system.
- Apparent angle subtended by a source above which the thermal hazard is proportional to the radiance of the source ($\alpha_{\max}$): 100 mrad.
- Apparent angle subtended by a source above which the maximum permissible exposure (MPE) for extended sources applies ($\alpha_{\min}$): 1.5 mrad.
- Extended source correction factor (C_{E}) : $C_{\text{E}} = \alpha^2/(\alpha_{\max}\alpha_{\min}) = 267$.
- Wavelength correction factor (C_{B}) : $C_{\text{B}} = 10^{0.02(\lambda-450)} = 251$.
- Exposure duration beyond which the thermal MPE for an extended source is constant in terms of irradiance (T_2) : 100 s.

Since the PRF used for OR-PAM ophthalmic imaging is less than the critical frequency defined by ANSI (55 kHz for wavelengths between 0.4 and 1.05 μm), the MPE for OR-PAM ophthalmic imaging is subject to three ANSI rules [25].

Rule 1: Single Pulse Limit

The MPE for a single laser pulse is

$$\text{MPE}_{\text{SP}} = 5.0 C_{\text{E}} \times 10^{-7} = 1.33 \times 10^{-4} \left[\text{J/cm}^2\right]. \tag{2.10}$$

Rule 2: Average Power Limit

First, consider one B-scan. During each B-scan, the OR-PAM laser sends a pulse train containing 1,600 pulses with a PRF of 600 Hz. Since the B-scan exposure time (~2.7 s) is longer than 0.7 s and the wavelength is between 400 and 600 nm, dual limits due to both photochemical and thermal effects apply here. For photochemical effects, the MPE for the B-scan pulse train is

$$\text{MPE}_{\text{Bscan}}(\text{photochemical}) = 100 C_{\text{B}} \times \left(\frac{\pi}{4}\right) \alpha^2 \times 10^{-6} = 790 \left[\text{J/cm}^2\right]. \tag{2.11}$$

For thermal effects, the MPE for the B-scan pulse train is

$$\text{MPE}_{\text{Bscan}}(\text{thermal}) = 1.8 C_{\text{E}} T_{\text{Bscan}}^{0.75} \times 10^{-3} = 1.01 \left[\text{J/cm}^2\right]. \tag{2.12}$$

Thus, the MPE/pulse for the B-scan pulse train is

$$\frac{\text{MPE}_{\text{Bscan}}(\text{thermal})}{n_{\text{Bscan}}} = 6.3 \times 10^{-4} \left[\text{J/cm}^2\right]. \tag{2.13}$$

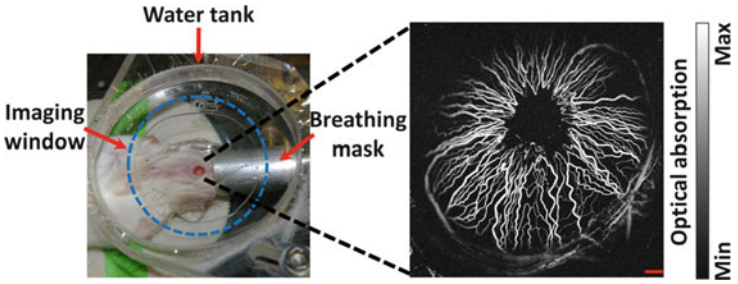

Fig. 2.6 In vivo optical-resolution photoacoustic microscopy of the anterior segment of a living mouse eye. (**a**) Photograph of the animal positioning. (**b**) Maximum-amplitude projection image acquired at 570 nm. Scale bar: 200 μm

Second, consider the total 2-h laser exposure. For photochemical effects, the MPE for the total exposure duration is the same as that for each B-scan [Eq. (2.11)]. For thermal effects, the MPE for the total exposure duration is

$$\mathrm{MPE}_{\mathrm{Total}}(\mathrm{thermal}) = 1.8 C_{\mathrm{E}} T_2^{-0.25} \times 10^{-3} \cdot T_{\max} = 1,093 \left[\mathrm{J/cm^2}\right]. \tag{2.14}$$

Thus, the MPE/pulse for the total 2-h laser exposure is

$$\frac{\mathrm{MPE}_{\mathrm{Total}}(\mathrm{photochemical})}{n_{\mathrm{Total}}} = 3.1 \times 10^{-4} \left[\mathrm{J/cm^2}\right]. \tag{2.15}$$

Rule 3: Repetitive Pulse Limit

The MPE for repetitive pulses is

$$\mathrm{MPE}_{\mathrm{RP}} = n_{\mathrm{Total}}^{-0.25} \mathrm{MPE}_{\mathrm{SP}} = 3.3 \times 10^{-6} \left[\mathrm{J/cm^2}\right]. \tag{2.16}$$

Rule 3 is the most conservative of the three. Therefore, the overall MPE for each pulse is $3.3 \times 10^{-6}\,\mathrm{J/cm^2}$. If the pupil diameter is 7 mm [25], the maximum permissible single laser pulse energy for OR-PAM ophthalmic imaging is computed to be 1.3 μJ. Thus, our experimentally used laser pulse energy (~40 nJ) is well within the ANSI limits. Figure 2.6 shows the animal positioning for ophthalmic OR-PAM imaging and a representative label-free OR-PAM image of the mouse iris microvasculature [11].

2.7.2 *Laser Safety for Skin Imaging [25]*

For skin imaging, a similar setting of experimental parameters as in the ophthalmic imaging has been used. Slightly differently, Rule 3 does not apply here. Typically, OR-PAM focuses ~200 μm beneath the skin surface with a focal diameter

of ∼5 μm. According to the geometry of a focused Gaussian beam, the beam diameter on the skin surface is ∼30 μm.

Rule 1: Single Pulse Limit

The MPE for a single laser pulse is

$$\mathrm{MPE_{SP}} = 2 \cdot C_\mathrm{A} \times 10^{-2} = 2.0 \times 10^{-2} \left[\mathrm{J/cm^2}\right], \tag{2.17}$$

where C_A, the wavelength correction factor, is unity when λ is between 400 and 700 nm.

Rule 2: Average Power Limit

Different from the anterior-eye-segment imaging, where all laser pulses overlap on the retina due to light defocusing, only ∼24 adjacent laser pulses overlap on the skin surface. With a PRF of 600 Hz, the exposure time t is 0.04 s. So, the MPE for the pulse train is

$$\mathrm{MPE_{train}} = 1.1 \cdot C_\mathrm{A} \cdot t^{0.25} = 0.5 \left[\mathrm{J/cm^2}\right]. \tag{2.18}$$

Thus, the MPE/pulse for the pulse train is

$$\frac{\mathrm{MPE_{average}} = \mathrm{MPE_{train}}}{24} = 2.1 \times 10^{-2} \left[\mathrm{J/cm^2}\right]. \tag{2.19}$$

Rule 1 is slightly more rigorous, so the overall MPE for each pulse is 2.0×10^{-2} J/cm^2. Knowing that the beam diameter on the skin surface is ∼30 μm, the maximum permissible single laser pulse energy for OR-PAM skin imaging is computed to be ∼141 nJ. Thus, our experimentally used laser pulse energy (∼40 nJ) is well within the ANSI limits.

2.8 Recent Technical Advances

Although traditional OR-PAM has demonstrated broad biomedical applications, its imaging speed is still slow compared with the mainstream optical microscopy technologies. Moreover, integration of OR-PAM with other optical microscopy for multicontrast imaging, as an original motivation for developing OR-PAM, has not been realized yet. Thus, recent technical developments of OR-PAM are focused on these two aspects.

2.8.1 New Scanning Mechanism

The integration of OR-PAM with existing optical microscopy has been hampered, mainly due to the incompatible scanning mechanisms. It is challenging to transplant the fast optical scanning widely used in optical microscopy technologies to OR-PAM, which requires scanning the ultrasonic-optical dual foci.

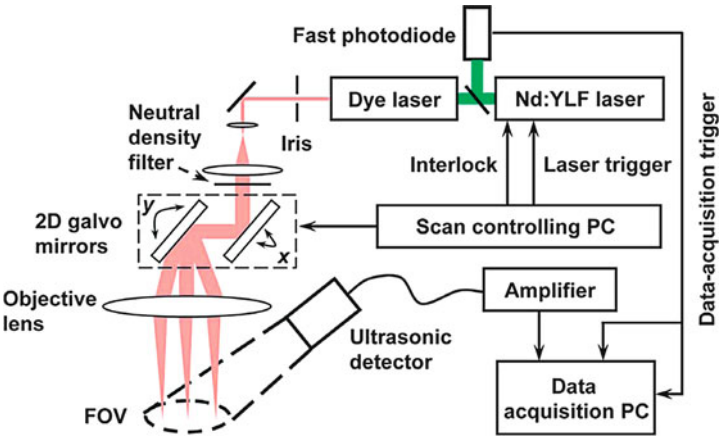

Fig. 2.7 Schematic of the laser-scanning optical-resolution photoacoustic microscopy setup

One intermediate solution is to relax the acoustic focus and keep it stationary, while the diffraction-limited optical focus is optically scanned inside the enlarged acoustic focus. This leads to the development of laser-scanning OR-PAM (LSOR-PAM) [26]. The configuration of the LSOR-PAM system is similar to that of the traditional mechanical-scanning-based OR-PAM (Fig. 2.7). The pulsed laser beam generated from the same type of wavelength-tunable laser system is spatially filtered by an iris, and the beam diameter is expanded to 8 mm by a pair of condenser lens. The expanded laser beam is then attenuated and steered by a 2-D galvanometer scanner (6230H, Cambridge Technology) before entering an objective lens (AC254-060-A1, Thorlabs) for optical focusing. An unfocused ultrasonic transducer (V312, Olympus NDT; center frequency: 10 MHz; bandwidth: 80%; active element diameter: 6 mm) is placed 30 mm away from the object with an oblique angle of ~15°, which allows to overlap the optical illumination without blockage.

LSOR-PAM enables fast scanning with designable scanning patterns, which is particularly useful when studying the behavior of a single microvessel. However, unlike traditional OR-PAM, LSOR-PAM has a limited field of view (FOV) (6 mm in diameter in this case), which is determined by the ultrasonic beam size of the unfocused transducer. Moreover, the SNR of LSOR-PAM is lower than that of traditional OR-PAM because of the reduced sensitivity of the unfocused ultrasonic transducer at the optical focus.

To improve the imaging speed of OR-PAM while maintaining a high SNR, Rao et al. developed a hybrid-scanning OR-PAM (HSOR-PAM) system [27]. In HSOR-PAM (Fig. 2.8), the pulsed laser beam is scanned along the B-scan direction by a one-dimensional (1-D) galvanometer scanner (6220H, Cambridge Technology). A glass plate is submerged in the water tank to reflect the photoacoustic waves to a cylindrically focused ultrasonic transducer (25 MHz bandwidth, focal length 15 mm,

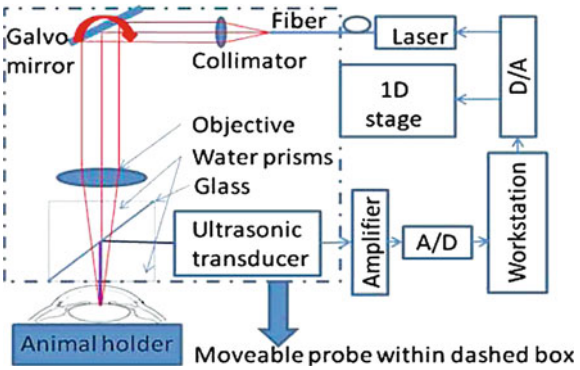

Fig. 2.8 Schematic of the hybrid-scanning optical-resolution photoacoustic microscopy system

material PZT, GE). The transducer has a line focus and thus frees acoustic scanning in the B-scan direction. The entire imaging head is mechanically scanned by a 1-D translation stage to form a volumetric image. The HSOR-PAM system operates at an imaging speed of 5,000 A-lines/s, with a slightly degraded SNR (5 dB lower) compared with traditional OR-PAM.

2.8.2 Integration with Optical Coherence Tomography

Recently, Li et al. reported the first combined system integrating transmission-mode OR-PAM with spectral-domain OCT [28]. In this combined system (Fig. 2.9), OR-PAM and OCT share the same single-mode fiber (P1-630A-FC-2, Thorlabs) for light delivery and the same microscope objective (E1, Leica) for optical illumination. Two-dimensional mechanical scanning of the object platform, in combination with the depth-resolved optical/ultrasonic detection, provides volumetric OCT/OR-PAM images.

Although the present imaging system demonstrates the feasibility of integrating OR-PAM with OCT, the relatively slow mechanical scanning limits its practical values. Taking advantage of the recently developed LSOR-PAM technology, Jiao et al. developed a combined laser-scanning-based OR-PAM and OCT system [29]. Figure 2.10 shows a schematic of the combined system. The configuration of the LSOR-PAM subsystem is the same as the one shown in Fig. 2.7. To incorporate the OCT subsystem, a dichroic mirror (NT43-955, Edmund Optics) is inserted right before the 2-D galvanometer (QS-10, Nutfield Technology). The passband of the dichroic mirror is carefully chosen to ensure a perfect reflection of the OCT beam and a maximized transmission of the OR-PAM beam. Then, the combined OCT and OR-PAM beams are focused into the object by an achromatic lens (AC254-060-A1, Thorlabs) and optically scanned by the galvanometer to form co-registered OCT and OR-PAM images.

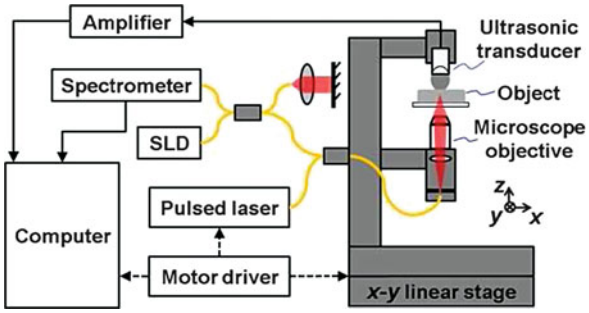

Fig. 2.9 Schematic of the combined optical-resolution photoacoustic microscopy and optical coherence tomography system

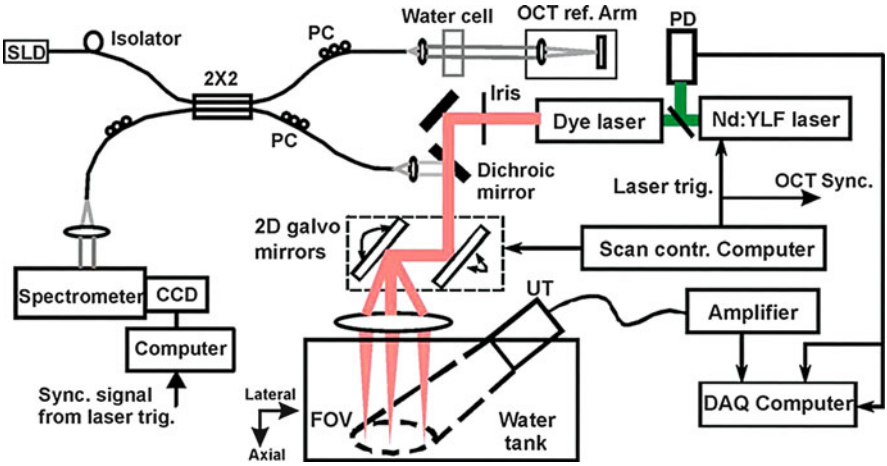

Fig. 2.10 Schematic of the integrated laser-scanning optical-resolution photoacoustic microscopy and optical coherence tomography system

Besides OCT, OR-PAM has also been integrated with confocal fluorescence microscopy to image the dual contrasts of optical absorption and molecular fluorescence simultaneously [30]. Combining OR-PAM with other optical microscopy provides fruitful anatomical, functional, and molecular information and is invaluable for both biological research and clinical diagnosis.

2.9 An Example Application: Wound Healing Monitoring

OR-PAM, capable of label-free imaging of multiple important vascular parameters (vascular morphology, HbT, sO_2, and blood flow) in a variety of in vivo anatomical sites (skin, eye, and brain), holds broad applications in circulation-related

physiological, pathophysiological, and clinical studies. Here, we only highlight the longitudinal monitoring capability of OR-PAM, which enables real-time study of disease progression and drug functioning. More biomedical applications of OR-PAM can be found in the literature [8, 10, 11, 13, 16, 31].

For technical demonstration, OR-PAM monitored the healing process of a laser-induced microvascular lesion in a mouse ear model [9]. Commercial transmission-mode optical microscopy was also used to monitor the same process, as a reference to OR-PAM. At the beginning of the chronic imaging, a $1 \times 1\,\text{mm}^2$ ROI in the mouse ear (Hsd:Athymic Nude-Foxn 1^{NU}, Harlan; body weight: $\sim$25 g) was selected and photographed by the transmission-mode optical microscope, after which the ROI was imaged by dual wavelengths (570 and 578 nm) OR-PAM [Fig. 2.11A]. Then, we switched to a continuous-wave laser (MGL-III-532, Changchun New Industries; output power: 150 mW, wavelength: 532 nm), removed the pinhole, and scanned the central part of the ROI ($0.25 \times 0.25\,\text{mm}^2$) with the focused laser beam (diameter: $\sim$30 μm) for $\sim$10 min to create a microvascular lesion. The ROI was imaged immediately after the laser destruction [Fig. 2.11B] and in the subsequent 12 days [Fig. 2.11C-1 to C-12]. Our results clearly show a four-step wound healing process that has been documented in physiology books [32]:

1. Vessel regression and hemostasis occurred right after the laser destruction [Fig. 2.11B].
2. Vasodilation was induced by inflammation 1 day after the injury and lasted for about 5 days [Figs. 2.11C-1 to C-5]. Tissue hypoxia occurred right after the laser destruction to trigger angiogenesis [Figs. 2.11B and C-1 to C-5].
3. The ingrowth of neocapillaries started to restore the microcirculation 3 days after the wound occurred [Fig. 2.11C-3].
4. The damaged arteriole-venule pair recovered morphologically and functionally after 12 days [Fig. 2.11C-12].

Note that, as an enabling technology for noninvasive label-free longitudinal monitoring of microhemodynamics, OR-PAM has potentially broader applications. In vascular physiological study, OR-PAM can help understand the signaling pathway of vascular regulation by perturbing the pathway and monitor the consequential anatomical and functional changes [31]. In cancer research, OR-PAM can monitor tumor neovascularization and evaluate cancer therapy. In vascular-related drug development, OR-PAM can trace drug functioning and evaluate drug efficacy. In laser microsurgery, surgical lasers can be readily integrated with OR-PAM to perform on-site high-precision microsurgery with presurgery diagnosis and postsurgery evaluation. In neuroscience, the minimally invasive feature of OR-PAM is ideal for chronic studies of cortical plasticity and neurovascular coupling at the capillary level.

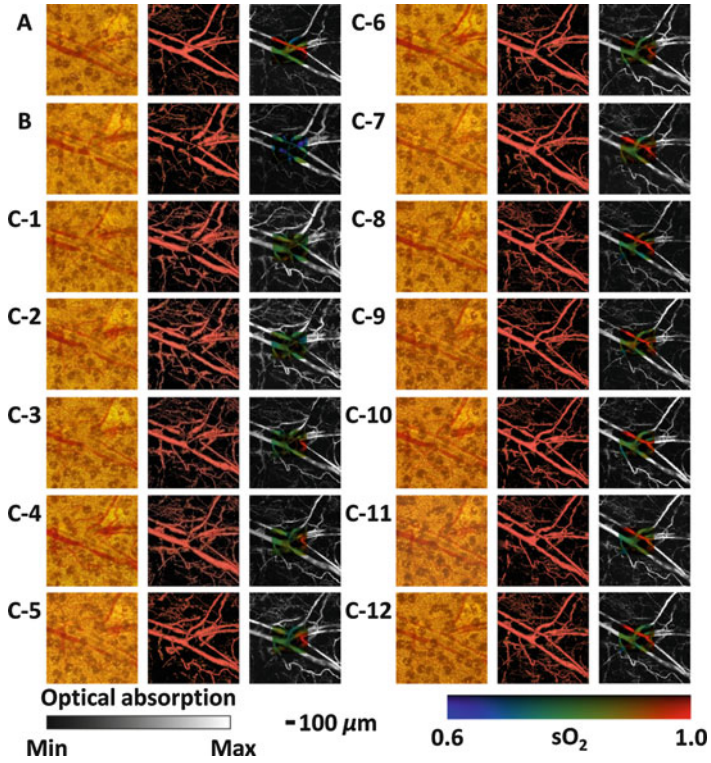

Fig. 2.11 Optical-resolution photoacoustic microscopy (OR-PAM) of the healing process of a laser-induced microvascular lesion (A) before laser destruction, (B) immediately after laser destruction, and (C) on each of the subsequent 12 days. The left image in each panel is the photograph taken by a commercial transmission-mode optical microscope; the middle image is the front view of the 3-D microvascular morphology acquired by OR-PAM at 57 nm; the right image is the maximum-amplitude projection image overlaid by the hemoglobin oxygen saturation map of the laser-damaged region

2.10 Perspectives

OR-PAM has potentially broad applications in biomedical imaging, yet much effort still needs to be invested to mature this technology. Four potential directions of future OR-PAM development are anticipated:

- Fast scanning over a large FOV. The current fast scanning strategy (i.e., optical scanning) limits the FOV to less than 6 mm, which is inadequate in many applications. One possible solution is to increase the speed of mechanical scanning by using specific scanners [33].
- Optical detection of photoacoustic waves. Current acoustic detection in OR-PAM is based on piezoelectric transducers, which require good tissue contact and

generally involve water in acoustic coupling. This configuration leads to system complexity and experimental inconvenience. Moreover, the detection sensitivity of the transducer falls off with its element size. Higher detection frequency is achieved at the expense of SNR. To overcome these limitations, noncontact optical methods for ultrasonic detection need to be explored.

- Integrating OR-PAM with AR-PAM for multiscale imaging. As shown in Fig. 2.1, OR-PAM and AR-PAM are highly complementary in terms of spatial resolution and tissue penetration. Combining them together would enable users to select an optimal trade-off between the spatial resolution and the penetration depth for different applications.
- Integrating OR-PAM with multiphoton fluorescence microscopy for neurovascular imaging. OR-PAM and multiphoton microscopy have similar penetration depths in soft brain tissues [8]. Combining them would enable direct visualization of the interaction between neuron activities and vascular dynamics.

Being one of the most actively studied optical microscopy technologies, OR-PAM has experienced a dramatic development within the last few years. We are looking forward to see OR-PAM in the mainstream.

Acknowledgements This work was sponsored by National Institutes of Health Grants R01 EB000712, EB000712A2S1, R01 EB00071207S2, R01 EB008085, R01 CA113453901, U54 CA136398, and 5P60 DK02057933. Professor Lihong V. Wang has a financial interest in Microphotoacoustics, Inc. and Endra, Inc., which, however, did not support this work.

Animal Ethics

All experimental animal procedures were carried out in conformance with the laboratory animal protocol approved by the School of Medicine Animal Studies Committee of Washington University in St. Louis.

References

1. S. Hu, L.V. Wang, Photoacoustic imaging and characterization of the microvasculature. J. Biomed. Opt. **15**, 011101(2010)
2. L.V. Wang, H. Wu, *Biomedical Optics: Principles and Imaging*. (Wiley, Hoboken, 2007)
3. X. Wang, Y. Pang, G. Ku, X. Xie, G. Stoica, L.V. Wang, Noninvasive laser-induced photoacoustic tomography for structural and functional in vivo imaging of the brain. Nat. Biotechnol. **21**, 803–806 (2003)
4. K. Maslov, G. Stoica, L.V. Wang, In vivo dark-field reflection-mode photoacoustic microscopy. Opt. Lett. **30**, 625–627 (2005)
5. H.F. Zhang, K. Maslov, G. Stoica, L.V. Wang, Functional photoacoustic microscopy for high-resolution and noninvasive in vivo imaging. Nat. Biotechnol. **24**, 848–851 (2006)
6. K. Maslov, H.F. Zhang, S. Hu, L.V. Wang, Optical-resolution photoacoustic microscopy for in vivo imaging of single capillaries. Opt. Lett. **33**, 929–931 (2008)

7. K. Maslov, G. Ku, L.V. Wang, Photoacoustic microscopy with submicron resolution. Proc. SPIE **7564**, 75640W (2010)
8. S. Hu, K. Maslov, V. Tsytsarev, L.V. Wang, Functional transcranial brain imaging by optical-resolution photoacoustic microscopy. J. Biomed. Opt. **14**, 040503 (2009)
9. S. Hu, K. Maslov, L.V. Wang, In vivo functional chronic imaging of a small animal model using optical-resolution photoacoustic microscopy. Med. Phys. **36**, 2320–2323 (2009)
10. S. Hu, K. Maslov, L.V. Wang, Noninvasive label-free imaging of microhemodynamics by optical-resolution photoacoustic microscopy. Opt. Express **17**, 7688–7693 (2009)
11. S. Hu, B. Rao, K. Maslov, L.V. Wang, Label-free photoacoustic ophthalmic angiography. Opt. Lett. **35**, 1–3 (2010)
12. S. Hu, L.V. Wang, Neurovascular photoacoustic tomography. Front. Neuroenerg. **2**, doi:10.3389/fnene.2010.00010 (2010)
13. S. Hu, P. Yan, K. Maslov, J.M. Lee, L.V. Wang, Intravital imaging of amyloid plaques in a transgenic mouse model using optical-resolution photoacoustic microscopy. Opt. Lett. **34**, 3899–3901 (2009)
14. S.L. Jiao, M.S. Jiang, J.M. Hu, A. Fawzi, Q. Zhou, K.K. Shung, C.A. Puliafito, H.F. Zhang, Photoacoustic ophthalmoscopy for in vivo retinal imaging. Opt. Express, **18**, 3967–3972 (2010)
15. J.J. Yao, K.I. Maslov, Y.F. Shi, L.A. Taber, L.V. Wang, In vivo photoacoustic imaging of transverse blood flow by using Doppler broadening of bandwidth. Opt. Lett. **35**, 1419–1421 (2010)
16. S. Hu, K. Maslov, L.V. Wang, Optical-resolution photoacoustic microscopy for in vivo imaging of microvasculature. Tuchin, V. V. (Ed.), *Handbook of Photonics for Biomedical Science* (CRC Press, 2010)
17. E.W. Stein, K. Maslov, L.V. Wang, Noninvasive mapping of the electrically stimulated mouse brain using photoacoustic microscopy. Proc. SPIE **6856**, 68561J (2008)
18. K. Maslov, H.F. Zhang, S. Hu, L.V. Wang, Optical-resolution confocal photoacoustic microscopy. Proc. SPIE **6856**, 68561I (2008)
19. H.F. Zhang, K. Maslov, M. Sivaramakrishnan, G. Stoica, L.V. Wang, Imaging of hemoglobin oxygen saturation variations in single vessels in vivo using photoacoustic microscopy. Appl. Phys. Lett. **90**, 3 (2007)
20. S.L. Jacques, S.A. Prahl, http://omlc.ogi.edu/spectra/hemoglobin/index.html
21. H. Fang, K. Maslov, L.V. Wang, Photoacoustic Doppler effect from flowing small light-absorbing particles. Phys. Rev. Lett. **99**, 184501 (2007)
22. H. Fang, K. Maslov, L.V. Wang, Photoacoustic Doppler flow measurement in optically scattering media. Appl. Phys. Lett. **91**, 3 (2007)
23. H. Fang, L.V. Wang, M-mode photoacoustic particle flow imaging. Opt. Lett. **34**, 671–673 (2009)
24. J. Yao, L.V. Wang, Transverse flow imaging based on photoacoustic Doppler bandwidth broadening. J. Biomed. Opt. **15**, 021303 (2010)
25. American National Standards Institute Inc., New York, NY (2007)
26. Z. Xie, S. Jiao, H.F. Zhang, C.A. Puliafito, Laser-scanning optical-resolution photoacoustic microscopy. Opt. Lett. **34**, 1771–1773 (2009)
27. B. Rao, L. Li, K. Maslov, L.V. Wang, Hybrid-scanning optical-resolution photoacoustic microscopy for in vivo vasculature imaging. Opt Lett, **35**, 1521–1523 (2010)
28. L. Li, K. Maslov, G. Ku, L.V. Wang, Three-dimensional combined photoacoustic and optical coherence microscopy for in vivo microcirculation studies. Opt. Express **17**, 16450–16455 (2009)
29. S. Jiao, Z. Xie, H.F. Zhang, C.A. Puliafito, Simultaneous multimodal imaging with integrated photoacoustic microscopy and optical coherence tomography. Opt. Lett. **34**, 2961–2963 (2009)
30. Y. Wang, K. Maslov, C. Kim, S. Hu, L.V. Wang, Integrated photoacoustic and fluorescence confocal microscopy. IEEE Trans. Biomed. Eng. **57**(10), 2576–2578 (2010)

31. S. Hu, J. Yao, K. Maslov, L.V. Ang, S. Oladipupo, A.C. Santeford, J. Kovalski, J.M. Arbeit, Optical-resolution photoacoustic microscopy of angiogenesis in a transgenic mouse model. Proc. SPIE **7564**, 756406 (2010)
32. A.F. Falabella, R.S. Kirsner, *Wound Healing* (Talyor & Francis, Boca Raton, 2005)
33. T. Harrison, J.C. Ranasinghesagara, H. Lu, K. Mathewson, A. Walsh, R.Z. Zemp, Combined photoacoustic and ultrasound biomicroscopy. Opt. Express **17**, 22041–22046 (2009)

http://www.springer.com/978-3-642-28390-1

Biomedical Optical Imaging Technologies
Design and Applications
Liang, R. (Ed.)
2013, XIV, 382 p., Hardcover
ISBN: 978-3-642-28390-1